



1

2

3

4

5

6

7

8

9

10

11

12

13

14

15

16

Revisited heat budget and probability distributions of turbulent heat fluxes in the Mediterranean Sea

Mahmud Hasan Ghani¹, Nadia Pinardi^{1,2}, Antonio Navarra^{2,3}, Lorenzo Mentaschi^{1,2},
Silvia Bianconcini⁴, Francesco Maicu², and Francesco Trotta²

¹ Dept. of Physics and Astronomy, University of Bologna, Bologna, Italy

² CMCC Foundation - Euro-Mediterranean Center on Climate Change, Italy

³ Dept. of Biological, Geological and Environmental Sciences, University of Bologna, Bologna, Italy

⁴ Dept. of Statistics, University of Bologna, Bologna, Italy

Corresponding author: Mahmud Hasan Ghani, mahmudhasan.ghani2@unibo.it



Abstract

17

18

19 Understanding the surface heat budget of the Mediterranean Sea is essential for assessing its role in regional climate
20 and ocean circulation. Under the steady-state heat budget closure hypothesis, the Mediterranean should exhibit a
21 net surface heat loss to balance the heat gained through the inflow of warm Atlantic water at the Gibraltar Strait.
22 However, literature estimates of the net heat flux vary widely, raising questions about the accuracy of existing
23 reanalysis products. In this study, we compute the net surface heat flux over the Mediterranean using two
24 atmospheric datasets: high-resolution (0.125°) ECMWF analysis and lower-resolution (0.25°) ERA5 reanalysis. By
25 applying the same sea surface temperature fields and bulk formulas in both cases, we isolate the impact of
26 atmospheric resolution and data quality. We find that the ECMWF analysis yields a basin-averaged net heat flux
27 of $-3.6 \pm 1.3 \text{ W m}^{-2}$, consistent with the closure hypothesis, while ERA5 gives a spurious positive flux of
28 $+5 \pm 1.2 \text{ W m}^{-2}$. Furthermore, beyond simply assessing the net heat budget, this study delves into the probability
29 distributions of air-sea heat fluxes, aiming to gain a deeper understanding of associated uncertainties and extreme
30 values in turbulent heat fluxes. The probability distributions for turbulent heat flux components exhibit
31 characteristics such as skewness and kurtosis, respectively, varying across the basin. To assess the influence of
32 extremes, we apply the Interquartile Range (IQR) method within statistical models that account for the skewed
33 nature of turbulent heat flux distributions, enabling a consistent treatment of outliers. Our results reveal that extreme
34 negative heat flux events play a critical role in determining the net heat flux direction; excluding these extremes
35 leads to a spurious positive heat budget. This highlights the importance of high-resolution atmospheric data for
36 accurately capturing air-sea interactions and ensuring physically consistent climate modelling over the
37 Mediterranean Sea. And we demonstrate that the Mediterranean heat budget closure hypothesis is connected to
38 extreme heat loss events occurring in key regions of the basin, such as the Gulf of Lion, the Adriatic Sea, the Aegean
39 Sea, and the southern Turkish coasts.

40 KEYWORDS: Heat fluxes, Mediterranean net heat budget, Fluxes probability distributions, heat flux extremes

41



42 1. Introduction

43

44 The exchange of momentum, water, and heat between the atmosphere and ocean plays a pivotal role in connecting
45 their dynamics (Kara et al., 2000). These fluxes, influenced by atmospheric surface variables and Sea Surface
46 Temperature (SST), drive ocean circulation (Large and Yeager, 2009; Small et al., 2019).

47 Our study focuses on the Mediterranean Sea, a unique semi-enclosed anti-estuarine basin where heat, water, and
48 momentum fluxes intertwine to fuel a robust vertical circulation (Pinardi et al., 2019). We aim to reassess the long
49 term mean net heat flux of the basin since this flux is a source of energy for the basin wide circulation (Cessi et al.,
50 2014). Moreover, the Mediterranean net heat budget comprises of several terms that show a considerable range of
51 uncertainty due to large temporal uncertainties arises from the surface fluxes (Jordà et al., 2017).

52 Understanding the heat balance in the Mediterranean Sea has long been a formidable task (Bignami et al., 1995;
53 Castellari et al., 1998; Matsoukas et al., 2005; Pettenuzzo et al., 2010; Sanchez-Gomez et al., 2011; Criado-
54 Aldeanueva et al., 2012; Jordà et al., 2017), whether through numerical models or observational data analysis. The
55 fundamental problem of in-situ observations is the limited space-time extension of the data sets, while for numerical
56 modelling, the limitations lie in the semi-empirical approach of the air-sea bulk formulas. Numerous endeavours
57 have been undertaken (Large and Yeager, 2009) to calculate air-sea heat fluxes using atmospheric state variables
58 obtained from in-situ observations, remote sensing data, or numerical model outputs. In our study, we utilize
59 atmospheric analysis and reanalysis data, which provide an optimal reconstruction of past atmospheric surface state
60 variables using models and observations.

61 Numerous past studies have employed well-established bulk transfer formulas to estimate air-sea fluxes (e.g., Fairall
62 et al., 2003; Pettenuzzo et al., 2010; Cronin et al., 2019). The turbulent heat flux components-latent and sensible
63 heat flux are commonly derived from surface wind speed, sea surface temperature, near-surface air temperature,
64 and humidity (Large and Yeager, 2009). However, Gulev and Belyaev (2012) noted that global heat flux products
65 often vary significantly, mainly due to differences in the bulk formulations and input variables adopted across
66 studies.

67 At the Gibraltar Strait, the Mediterranean Sea exchanges water with the Atlantic through a characteristic two-layer
68 flow: warm, relatively fresh Atlantic water enters at the surface, while colder, saltier Mediterranean water exits at
69 depth. This arrangement leads to a net gain of heat for the Mediterranean basin, since the incoming surface water
70 carries more thermal energy than the colder outflow. To maintain a long-term heat balance, this lateral heat gain
71 must be compensated by a net loss of heat at the sea surface. In other words, the basin-average surface heat flux
72 should be negative-a constraint known as the heat budget closure hypothesis. Accurately estimating this surface
73 heat flux remains a challenge due to limited data and uncertainties in flux parameterizations. A benchmark estimates
74 of the net heat budget, -7 W m^{-2} , was proposed by Béthoux et al. (1998), though it is based on data from the 1970s
75 and 1980s and may not reflect present-day conditions under a changing climate (Criado-Aldeanueva et al., 2012;
76 Marullo et al., 2021).

77 Recent studies highlight significant uncertainty in the estimated long-term net heat budget of the Mediterranean Sea,
78 with some even reporting positive values. Song and Yu (2017), presented an ensemble climatology of surface heat
79 fluxes, reporting a net heat budget of $2 \pm 12 \text{ W m}^{-2}$ and noting a warm bias in this ensemble estimate. Utilizing an



80 ensemble of high-resolution regional climate models (RCMs), Sanchez-Gomez et al. (2011) found that individual
81 RCMs did not achieve a heat budget closure, but the ensemble mean heat flux was $-7 \pm 21 \text{ W m}^{-2}$. Ruiz et al. (2008)
82 achieved a heat budget of -1 W m^{-2} using downscaled NCEP/NCAR global reanalysis of $\frac{1}{2}^\circ \times \frac{1}{2}^\circ$ resolution, but
83 their computed heat flux components values have shown large deviation than most of the literature values (the major
84 difference is in the value of 168 W m^{-2} for net short wave downward). Merullo et al. (2021) recently analysed
85 several atmospheric data sets, revealing a significant net heat flux variability ranging between 1.6 and 40 W m^{-2} .
86 They attributed this variability primarily to longwave radiation fluxes uncertainties. In addition to these challenges,
87 past studies of air-sea fluxes have primarily focused on establishing mean and variance, leaving limited knowledge
88 about their statistical distributions (Korolev et al., 2015; Tian et al., 2017). Understanding the probability
89 distributions of air-sea fluxes and their higher moments could provide insights into the uncertainties associated with
90 air-sea physics. Also, the analysis of probability distributions can help to assess skills of different reanalyses to
91 replicate extreme fluxes (Gulev and Belayaev, 2012).

92 In this study we investigate two very different aspects of the net surface heat budget closure problem of the
93 Mediterranean Sea. First, we employ two different by high quality surface atmospheric variable data sets at different
94 horizontal resolution and we calculate the heat fluxes with the same bulk formula and the same SST. This isolates
95 the impact of atmospheric model resolution and quality as the sole source of variation in the heat flux estimates.
96 Therefore, we answer the question: is the Mediterranean Sea in the past 15 years still losing heat at the surface?

97 Secondly, we study the statistical distributions of the heat flux components, utilizing the atmospheric analysis dataset
98 which are used to produce weather forecast by ECMWF (European Centre for Medium-Range Weather Forecasts).
99 Knowing the skewness and kurtosis distributions across the basin, we analyse the extremes of the net heat budget,
100 and we determine the specific importance of the extreme heat losses to the long-term mean. The second question
101 we answer is: what are the underlying causes of the net heat budget closure problem?

102 The paper is structured into the following sections. Section 2 presents the atmospheric analysis and reanalysis
103 datasets from ECMWF, along with satellite SST data and the bulk formula used in the estimation of the fluxes. In
104 Section 3, we present the new values of the heat budget closure problem, compared to the literature. In section 4,
105 we analyse the probability distributions of turbulent heat fluxes. In Section 5, we determine the causes of the long
106 term mean net heat budget values. Finally, Section 6 summarizes the findings and highlights key insights gleaned
107 from this research.

108

109 **2. Methodology and datasets**

110 **2.1 Air-sea physics in the Mediterranean Sea**

111 For the Mediterranean Sea, several formulations have been established over the past decades through extensive
112 studies. In this section, we present these adopted formulations, beginning with the net heat flux formula, followed
113 by the specific heat flux components utilized in this study.



The net surface heat flux, Q_{net} comprises the net shortwave radiation Q_{SW} , net longwave radiation Q_{LW} , and surface turbulent flux components, which encompass the latent heat flux of evaporation Q_{LH} and sensible heat flux Q_{SH} (Cronin et al., 2019; Pettenuzzo et al., 2010).

$$Q_{net} = Q_{SW} + Q_{LW} + Q_{lat} + Q_{sen} \quad (1)$$

Here, we use the convention that positive heat fluxes denote heat gain by the ocean. We did not use directly the atmospheric model heat flux values since we wanted to intercompare two different atmospheric data sets in terms of their quality and resolution not on the basis of the specific bulk parametrizations and SST used. Thus, we used the same bulk formula and SST for both ECMWF and ERA5 surface variables that are described in section 2.2.

2.1.1 Shortwave radiation flux

The shortwave radiation flux (SW) is derived from the formulation proposed by Rosati and Miyakoda (1988). The largest heat flux component is the solar radiation which is reduced by the cloud coverage and partially reflected by the sea surface (albedo). The shortwave heat flux formula is therefore expressed as:

$$Q_{SW} = Q_{TOT} (1 - 0.62 C + 0.0019 \beta)(1 - \alpha) \quad \text{if } C \geq 3 \quad (2)$$

$$Q_{SW} = Q_{TOT} (1 - \alpha) \quad \text{if } C < 3$$

where Q_{TOT} indicates the clear sky solar radiation calculated with astronomical formulae, C is the fractional cloud coverage, β is the noon solar altitude in degrees and α is the ocean surface albedo varying month wise values taken from Payne (1972). The incoming solar radiation varies on locations with sun zenith angel and Q_{TOT} reaches at the ocean surface after diffusion can be represented by the components: the sum of the direct solar radiation Q_{DIR} for direct solar radiation and Q_{DIF} for downward diffused radiation. Then net solar radiation Q_{TOT} can be represented by the summation of components Q_{DIR} and Q_{DIF} :

$$\begin{aligned} Q_{TOT} &= Q_{DIR} + Q_{DIF} \\ &= Q_0 \tau^{\sec z} + [(1 - A_a) Q_0 - Q_0 \tau^{\sec z}] * 0.5 \end{aligned}$$

Here Q_0 is the solar radiation at the top of atmosphere, τ is equal to 0.7 and is the atmospheric transmission coefficient, A_a is a constant value (0.09) and z is the sun zenith angle.



146 2.1.2 Longwave radiation flux

147 The longwave surface radiation flux (LW) is the difference between the upward infrared radiation (IR) emitted from
148 the ocean surface (LU) and the atmospheric downwelling infrared radiation (LD). The LD component is adapted
149 from Bignami et al. (1995), and the longwave radiation flux is written as:

150

$$151 \quad Q_{LW} = Q_{LU} + Q_{LD} \quad (3)$$

$$152 \quad Q_{LU} = -\epsilon \sigma_{SB} T_S^4 \quad (4)$$

$$153 \quad Q_{LD} = [\sigma_{SB} T_A^4 (0.653 + 0.00535 e_A)](1 + 0.1762 C^2) \quad (5)$$

154

155 where: T_S and T_A indicate the sea surface temperature and air temperature in degrees Kelvin, σ_{SB} is the Stefan-
156 Boltzmann constant, ϵ is the ocean emissivity set to 1 according to Large and Yager (2009) and e_A is the atmospheric
157 vapor pressure computed from the mixing ratio of the air W_{air} (Wallace and Hobbs, 2006).

$$158 \quad W_{air} = \frac{q_A}{1 - q_A} \quad (6)$$

$$159 \quad e_A = \frac{W_{air}}{(W_{air} + \gamma)} p \quad (7)$$

160 and q_A is the specific humidity of air, p is the surface air pressure, and γ is a constant (0.622).

161 The specific humidity (q_A) saturated at the T_A is computed using the following equation (Large, 2006)

$$162 \quad q_A = \rho^{-1} 640,380 \exp(-5107.4/T_D) \quad (8)$$

163 where, T_D is the dew point temperature retrieved from the atmospheric model outputs.

164

165 2.1.3 Turbulent heat fluxes

166 The turbulent heat flux is composed of sensible heat Q_{SH} and latent heat Q_{LH} given by the following formula:

$$167 \quad Q_{SH} = -\rho_A C_P C_H |\vec{V}| (T_S - T_A) \quad (09)$$

$$168 \quad Q_{LH} = -\rho_A L_E C_E |\vec{V}| (q_S - q_A) \quad (10)$$

169

170 where $|\vec{V}|$ is the wind speed, ρ_A is the density of moist air, C_P is the specific heat capacity ($1005 \text{ J g}^{-1} \cdot \text{K}$), C_H and
171 C_E are turbulent exchange coefficients for temperature and humidity, L_E is the latent heat of vaporization, q_A is
172 defined in (8) and q_S , which is the specific humidity of air saturated at the sea surface temperature T_S , is calculated
173 with (8) using T_S instead of T_D , and applying a 0.98 factor (Sverdrup, 1942). Since the average wind speed in the
174 Mediterranean is 5 m/s, Pettenuzzo et al. (2010) suggested using constant turbulent exchange coefficients such as
175 $C_H = 1.3 \cdot 10^{-3}$ and $C_E = 1.5 \cdot 10^{-3}$.

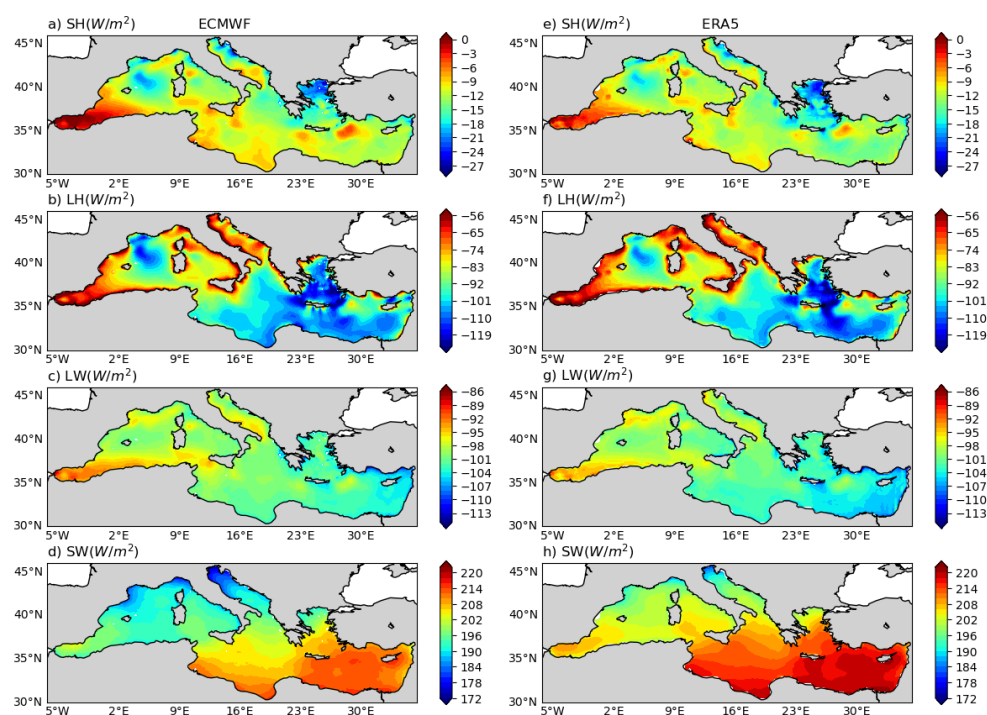


176 2.2 Datasets

177 Two atmospheric datasets have been selected for this study. The first dataset is the ECMWF (European Centre for
178 Medium-Range Weather Forecasts) high-resolution analysis dataset (Rabier et al., 2000) at six-hourly temporal
179 resolution and 0.125 degrees of spatial resolution. It's worth noting that the original operational dataset, from which
180 the atmospheric fields have been extracted, underwent changes between 1991 and 2006 in terms of model resolution
181 and the assimilated number of observations. For consistency, we opted to utilize the dataset with approximately
182 uniform model resolution and physics spanning a 15-year period from 2006 to 2020. The second dataset employed
183 in this study is ERA5 reanalysis (Hersbach et al., 2020). This dataset is available at hourly intervals. However, it
184 features a horizontal resolution of 0.25 degrees.

185 To mitigate unresolved atmospheric temperature daily cycles in ECMWF and make the two data sets consistent for
186 the time variability, the ECMWF and ERA5 fields are further processed into daily mean values for the entire period.
187 Comparisons conducted with daily and six-hourly input fields indicated minimal differences in the probability
188 distributions of the heat fluxes, leading us to prioritize filtering out daily variability to the greatest extent possible.

189 To compute the heat fluxes the following surface variables are extracted from the two datasets: the 10-meter wind
190 components (U for the zonal direction and V for the meridional direction), mean sea level pressure, dew point
191 temperature, total cloud coverage, and 2-meter air temperature.



192 **Figure 1: Mean annual heat flux components for the period of 2006-2020 computed from ECMWF (left) and**
193 **ERA5 (right) daily time series**
194

195



196 For the oceanic SST data, we utilized the satellite dataset distributed by the Copernicus Marine Environment Service
197 (CMEMS). This SST dataset is a blended product from multiple satellite sensors, categorized as L4, with a
198 horizontal resolution of $0.05^\circ \times 0.05^\circ$. To align the SST data with the atmospheric analysis and reanalysis dataset
199 grids, we applied an interpolation and extrapolation method known as the 'sea-over land' (De Dominicis et al., 2013).
200 This method involves an iterative process to extrapolate sea values over land before interpolating, thus not allowing
201 the contamination of land values on the interpolation.

202

203 **3. Heat budget closure problem revisited**

204 **3.1 Analysis of the heat budget components**

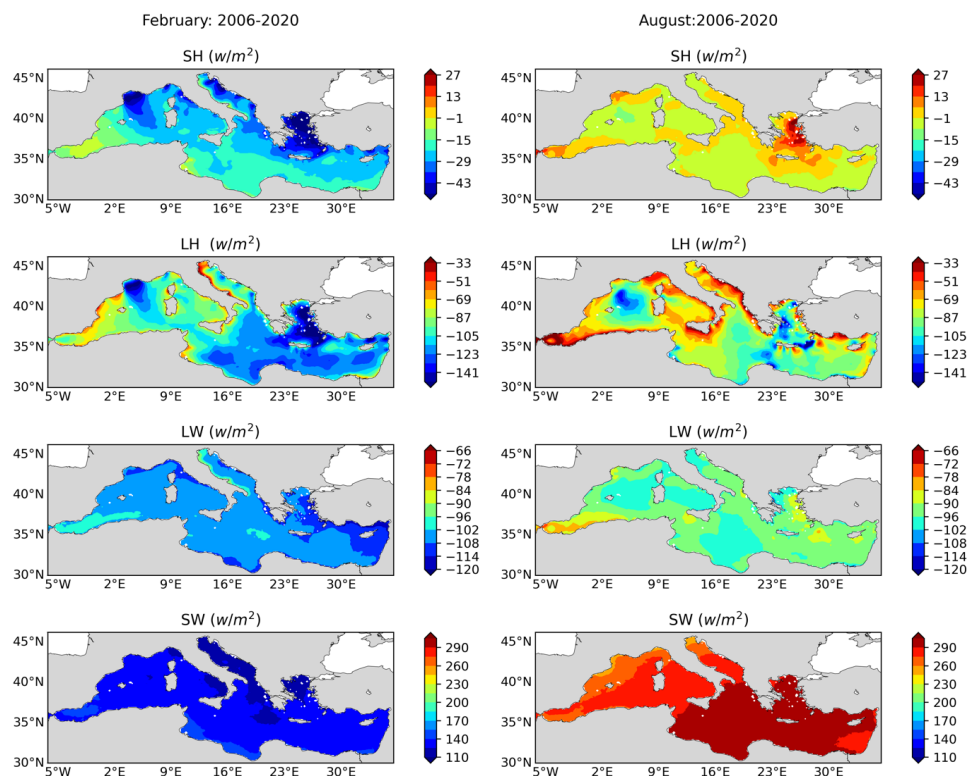
205

206 We compute the heat fluxes for the 15-year period, 2006–2020, using the ERA5 dataset and compare them with the
207 fluxes computed using the ECMWF dataset (Fig. 1). In Fig. 1 we show the results for the 15-year mean of each
208 heat budget components. We start describing the ECMWF patterns and then we detail the differences.

209 Turbulent heat fluxes exhibit distinct sub-basin-scale patterns, varying between the eastern and western
210 Mediterranean Seas as well as the Central Mediterranean region. The largest mean sensible heat loss is observed in
211 the whole Alboran sea area with absolute value range of $0\text{--}6\text{ W m}^{-2}$, while the Aegean Sea and the centre of Gulf of
212 Lion gains more heat in the maximum value of 25 W m^{-2} . Similarly, the highest absolute values of LH are recorded
213 in the Gulf of Lion and the Aegean and Levantine Seas, attributed to the influence of strong and cold winds like the
214 Mistral and Etesian in the north-western and eastern Mediterranean regions, respectively. The eastern
215 Mediterranean emerges as the region with the highest evaporation, reaching approximately 125 W m^{-2} in absolute
216 value. Notably, along the south-eastern coastline, a wide range of maximum absolute values ($102\text{--}125\text{ W m}^{-2}$) in
217 the evaporation is observed. The turbulent heat fluxes show limited differences between the ECMWF and ERA5
218 datasets.

219 SW fields show the well-known meridional gradients with larger gradient values arising from the ECMWF dataset.
220 The mean SW exhibits a gradual decline from the eastern to western Mediterranean, influenced by the variation of
221 the solar zenith angle with longitudes. The difference in SW radiation between the western and eastern
222 Mediterranean is suggestive of variations in cloud cover, leading to a larger heat gain in the eastern Mediterranean.
223 Furthermore, ECMWF and ERA5 different values are connected to different cloud cover. Notably, the northern
224 Adriatic region stands out with a distinct distribution, suggesting it receives relatively less annual solar radiation
225 compared to other areas. In contrast, the mean longwave (LW) radiation distribution maintains a relatively
226 consistent range of absolute values between $86\text{--}115\text{ W m}^{-2}$ across the entire domain with absolute minimum values
227 in the Alboran Sea, presumably due to the cold Atlantic water inflow. Overall, while the turbulent heat fluxes show
228 limited differences between the ECMWF and ERA5 datasets, significant discrepancies are observed in radiative
229 heat fluxes.

230



231

232 **Figure 2: Seasonal variations of heat flux components: Left column is the monthly average values for**
233 **February and right column the average for August for the period 2006-2020 (ECMWF data).**

234

235 Figure 2 shows seasonal variations in heat flux components for February and August using ECMWF data. Both SH
236 and latent heat (LH) fluxes exhibit a greater spatial gradient in February compared to August. In winter, the SH loss
237 is larger, especially in the Gulf of Lion, Aegean, and parts of the Adriatic, with stronger spatial gradients compared
238 to summer. In August, SH flux becomes positive in the Aegean and the Alboran Sea. LH loss is highest in February
239 in the whole eastern Mediterranean and the Gulf of Lion. In August, LH losses decrease in the western
240 Mediterranean, with absolute value minima in the Alboran and Adriatic Sea, remaining largely negative in the lower
241 part of in the Eastern Mediterranean. SW fields show the strongest seasonal cycle as expected, with the absolute
242 maximum summer of 290-320 W m⁻² in the Eastern Mediterranean. LW is largest in absolute value in winter
243 showing a small seasonal cycle. Significant seasonal variations are observed in the distribution range for radiative
244 heat fluxes, low in February and high in August across the entire domain. These patterns are quite similar to the
245 ones reported in the literature.

246

247



248 3.2 Net heat budget estimation

249

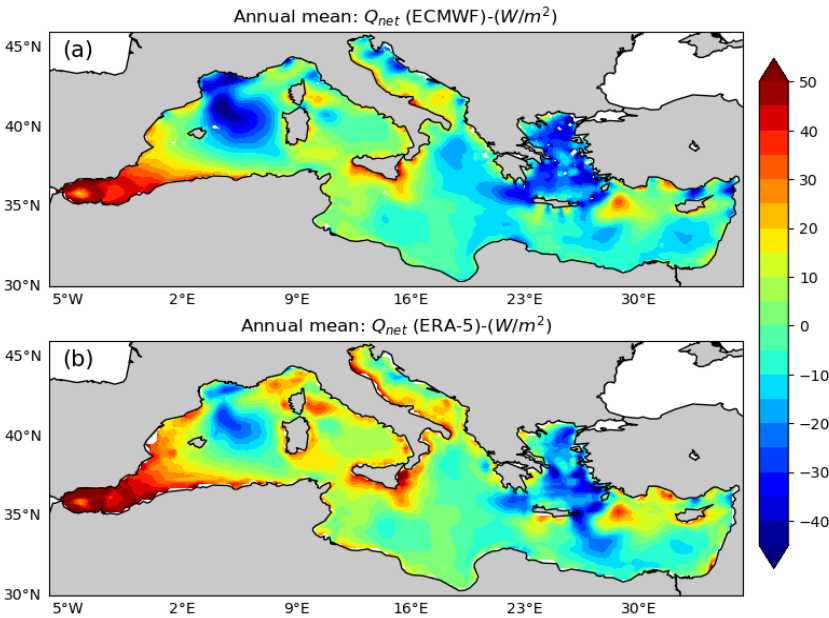
250 The net surface heat flux Q_{net} is depicted in Figure 3 for ERA5 and ECMWF and basin-average 15 year mean
251 values are listed together with the literature in Table 1.

252 Fig. 3 shows that the Gulf of Lion and the Aegean Sea are the areas of maximum heat losses while the basin gains
253 heat in the Alboran Sea, in some areas of the Levantine basin, and in the shelf areas around the Italian peninsula.

254 The Mediterranean Sea gains comparatively more heat with the ERA5 inputs. Besides the difference in surface
255 domain for Q_{net} , for both cases, air-sea flux dynamics is strongly visible in the Alboran Sea for net heat gain, in
256 the Gulf of Lion for heat loss due to the continental cold wind (Mistral wind), and in the Aegean Sea due to the
257 strong wind (Etesian wind) that blows during the summer period. Using ECMWF inputs, Q_{net} is -3.6 W m^{-2} , a
258 value consistent with previous estimates for the Mediterranean Sea domain and for ERA5, it is 5 W m^{-2} (Table 1).
259 Errors in Q_{net} mean value are determined by a bootstrapping method where Q_{net} time series is resampled 5000
260 times to compute a standard deviation around the mean of the resampled time series (Tibshirani & Efron, 1993).
261 We argue that our results show that the negative heat budget is achieved by using only ECMWF fields at high
262 resolution, i.e. 0.125 degrees. Higher resolution implies differences in all atmospheric fields used to compute the
263 fluxes. Furthermore, ERA5 and ECMWF model physics and dynamics is different contributing to the differences in
264 the mean heat budget. However, both datasets use observations, and we argue that the most relevant difference
265 between the analysis and the reanalysis data set is the resolution due to the peculiar geometry of the Mediterranean
266 Sea.

267 Since all the literature datasets are coarser, this is most likely the reason of the failure to determine the correct heat
268 budget closure value. In Pettenuzzo et al. (2010) several ad-hoc corrections were made to the surface atmospheric
269 fields to obtain the negative heat flux budget while in Sanchez-Gomes et al., (2011) they used an ensemble of
270 deterministically downscaled ERA40 fluxes giving rise to a very large uncertainty. Considering a recent literature,
271 our resulted Q_{net} is closely matched with the computed net heat budget of $-3 \pm 8 \text{ W m}^{-2}$ from Jordà et al., (2017), but
272 their result was associated to large temporal uncertainties from the surface fluxes through Gibraltar Strait.

273 Thus, comparing the net heat flux Q_{net} estimates derived from ERA5 reanalysis and ECMWF analysis dataset,
274 using specific bulk formula demonstrate an uncertainty in the results. This uncertainty, potentially linked to spatial
275 resolution difference between the two datasets, impacts the regional heat budget closure. We are now able to answer
276 the question: is the Mediterranean Sea in the past 15 years still losing heat at the surface? The answer is yes,
277 notwithstanding the climate change warming, the Mediterranean still loses heat due to its heat budget closure
278 constraint. However, it might be that it loses less than in the previous decades, and this will be the scope of more
279 studies in the future.



280

281 **Figure 3: Comparison of the annual Q_{net} ($W m^{-2}$) computed from, a) ECMWF and b) ERA-5 input datasets.**

282

283 **Table 1: Computed flux components and net heat fluxes (Q_{net}), and values from the references**

Authors	SH	LH	LW	SW	Net Flux (Q_{net})
Bethoux (1979)	-13	-120	-68	195	-6
Bunker (1982-1)	-13	-101	-68	202	20
Bunker et al (1982-2)	-11	-130	-68	202	20
May (1986)	-11	-130	-68	193	2
Garret et al. (1993)	-7	-99	-67	202	29
Matsoukas et al. (2005)	-11	-122	186	-63	22
Ruiz et al. (2008)	-8	-88	-73	168	-1
Pettenuzzo et al. (2010)	-14	-90	-79	178	-7
Sanchez-Gomez et al. (2011)	-13±5	-100±13	-75±6	181±18	-7±21
Criado-Aldeanueva et al. (2012)	-15.1	-93.5	-76.9	186.3	0.73
Song & Yoy (2017)	-13±4	-98±10	-78±13	192±19	2±12
Jordá, et al., 2017	-	-	-	-	-3±8
ECMWF analyses	-12.1±4	-92±16	-100.5±3	201±8	-3.6±1.3
ERA5 reanalysis	-13±3	-89±14	-101±3	208±8	5±1.2



Spatially, the mean Q_{net} distribution generally shows a heat loss across much of the Eastern Mediterranean. Overall, distributions of more positive net heat budget values for the western Mediterranean and negative for the eastern Mediterranean have matched with the similar result from Criado-Aldeanueva et al. (2012). Strong spatial gradients are evident, particularly in the Aegean Sea, although a few patches displaying net heat loss (negative Q_{net}) are also noticeable in this vicinity. Conversely, the western Mediterranean exhibits a stronger heat gain area, which appears particularly concentrated zone in the Gulf of Lion region and this feature is apparent in results from both atmospheric datasets. Such a spatial related uncertainty in Q_{net} represents a significant challenge for accurately closing regional heat budgets as well as validating existing ocean circulation models within the complex Mediterranean basin.

4. Probability distributions of the turbulent heat fluxes

In this section, we analyse the probability distribution of turbulent heat fluxes computed using ECMWF data set only and for the anomaly heat fluxes.

If we indicate the time series of each component of the heat budget with X_n we can define the heat flux climatology as:

$$Q_t = \frac{1}{n} \sum_{j=1}^n X_{tj} \quad (11)$$

where ‘t’ indicates the day of the year and ‘j’ is the number of years. The anomaly time series is computed by subtracting the long-term seasonal climatology Q_t from the observed heat flux time series X_{ij} and it will be indicated by:

$$\tilde{X}_{tj} = X_{tj} - Q_t \quad (12)$$

4.1 SH flux distribution

We found that gaussian or skew-normal distributions are not well fit for SH flux, as evident from the histograms at single grid points shown in Figure 4a. The histograms reveal a singularity around zero, indicating that the skew-normal distribution may not adequately capture the distribution of these values. This observation is consistent with findings by Gulev and Belyaev (2012), and we provide further explanation in the Appendix A.

The most common distribution with such near-discontinuous behaviour at the origin is the three-parameter Asymmetric Laplace Distribution (ALD) (Yu & Zhang, 2005) that we can defined as

$$F(x, \alpha, \mu, \lambda) = \frac{\lambda}{\alpha + 1} \begin{cases} \exp(\lambda/\alpha (x - \mu)) & \text{if } x < \mu \\ \exp(-\lambda \alpha (x - \mu)) & \text{if } x \geq \mu \end{cases} \quad (13)$$

where x is the random variable time series, α is the shape parameter, μ is the location and λ the scale.

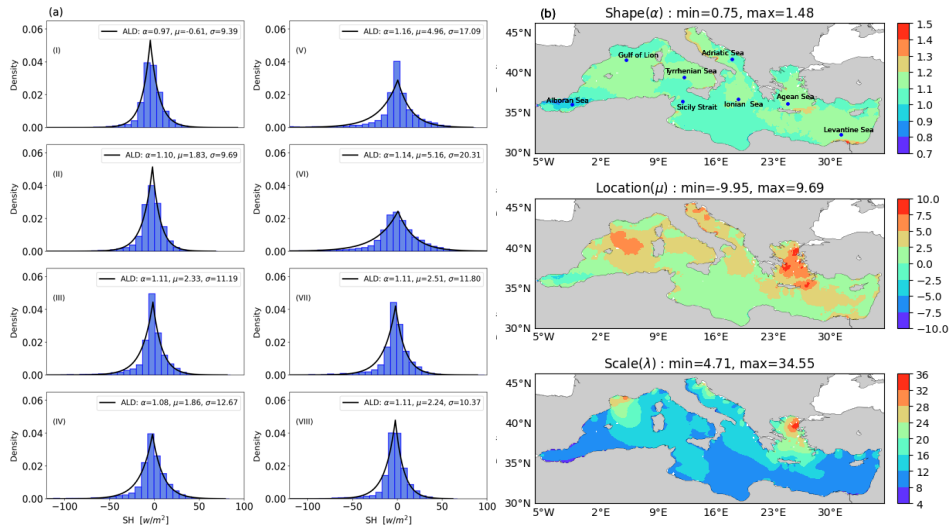


Figure 4 a) The single grid point histograms for SH flux anomalies from the eight sampling locations for the period of 2006-2020, 4 b) The Asymmetric Laplace PDF parameter (α , μ , λ) distributions from computed SH flux anomaly for the observation period. [Sampling points: (I) Alboran Sea, (II) Gulf of Lion, (III) Tyrrhenian Sea, (IV) Sicily Strait, (V) Adriatic Sea, (VI) Ionian Sea, (VII) Aegean Sea, (VIII) Levantine Sea]

From the single grid point histogram, we have observed a one or two sharp peaks in the distribution that matches well with the Asymmetric Laplace Distribution (ALD) PDF. In accordance with findings by Yu and Zhang (2005), the distribution of the sensible heat (SH) flux anomaly time series exhibits characteristics of a double exponential distribution. This is evident from the histograms displaying both positive and negative skewness with long tails, as depicted in Figure 4a. The ALD parameters for the SH flux anomaly time series are illustrated in Figure 4b. The shape parameter (α) falls within the positive range of 0.73 to 1.48, indicating a moderate to high degree of peakiness in the distribution. Additionally, the location parameter (μ) exhibits both positive and negative values, suggesting a shift in the central tendency of the distribution. Notably, the scale parameter (λ) displays a similar structure to the SH flux climatology depicted in Figure 1.

To check the quality of the fit, moments of both applied and theoretical PDF are compared (presented in supplementary materials, Fig. S3). The comparison shows the estimations of the three moments in the left panel for the observed SH flux and right panel for ALD PDF parameters. It can be seen that variances and skewness are similar in distribution while kurtosis differ at noticeable range. This observation is likely attributed to the fact that the kurtosis for the asymmetric Laplace distribution remains constant regardless of changes in the scale parameter.

4.2 LH flux distribution

In the case of the LH flux, no sharp exponential peaks were observed; instead, large skewness and long tails were identified. Therefore, we applied the skew-normal PDF which is defined by α ($\in \mathbb{R}$) as the shape parameter, μ ($\in \mathbb{R}$) the location parameter, and $\lambda > 0$ the scale parameter (Azzalini, 1985) and defined as:



$$f(x, \alpha, \mu, \lambda) = \frac{2}{\lambda} \phi\left(\frac{x-\mu}{\lambda}\right) \Phi\left(\alpha \frac{x-\mu}{\lambda}\right) \quad (14)$$

342

343 Where,

$$\phi\left(\frac{x-\mu}{\lambda}\right) = \frac{1}{\sqrt{2\pi}} e^{-\frac{1}{2} \frac{(x-\mu)^2}{\lambda^2}} \quad (15)$$

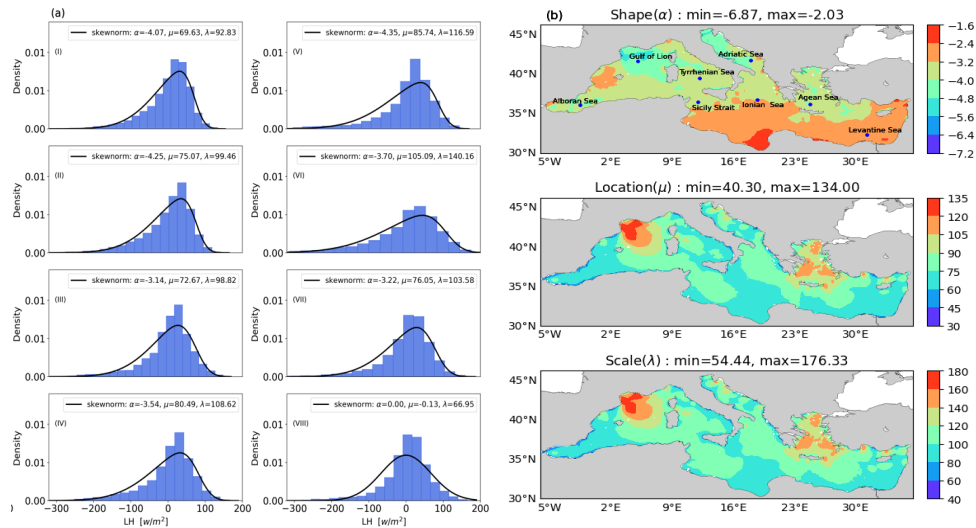
$$\Phi\left(\alpha \frac{x-\mu}{\lambda}\right) = \int_{-\infty}^{\alpha \frac{x-\mu}{\lambda}} \phi(t) dt \quad (16)$$

346 A skew-normal PDF is an extension of the normal distribution while covering the skewness and containing the
347 general characteristics of a Gaussian distribution (Flecher et al., 2010).

348 To examine visually the quality of PDF fit on LH flux anomaly values, histograms from eight sea locations were
349 fitted with the skew-normal PDF, as shown in Figure 5a. Figure 5b displays the parameter spatial variability. The
350 shape parameter distribution ranges from -6.83 to -2.5, with negative values observed across all points. This spatial
351 distribution of α , exhibiting a negative range, aligns with the negatively skewed pattern identified in the single grid
352 point PDF fitting test. Furthermore, the spatial distribution structure of the location and scale parameters
353 demonstrates a positive correlation across most locations.

354 In the Supplementary material, a comparison of statistical moments is conducted to qualitatively validate the fit
355 (supplementary materials, Fig S4). There is notable agreement in the variance distributions between the observed
356 LH flux anomaly and skew-normal PDF. While the skewness distributions mismatch at negligible level, with the
357 theoretical PDF skewness predominantly ranging from -0.9 to -0.3, whereas the observed skewness exhibits a
358 variation range spanning from -1.2 to over -0.3. Lastly, the kurtosis distribution of the skew-normal PDF differs in
359 the Aegean Sea, Alboran Sea and Gulf of Lion area.

360



361 **Figure 5 a) The single grid point histograms for LH flux anomalies at the eight sampling locations for the**
362 **period of 2006-2020, 5 b) The skew-normal PDF parameter (α, μ, λ) distributions for computed LH Flux**
363 **anomaly for the observation period [Sampling points: (I) Alboran Sea, (II) Gulf of Lion, (III) Tyrrhenian**
364 **Sea, (IV) Sicily Strait, (V) Adriatic Sea, (VI) Ionian Sea, (VII) Aegean Sea, (VIII) Levantine Sea]**



365 4.3 Evaluation of the PDF fitting

366 In this section, we conducted a goodness of fit test to measure the distance between the empirical observed
367 distribution and the fitted one. The objective of this evaluation test was to assess the degree of agreement between
368 the applied theoretical distribution and the observed time series. The chi-squared method, a well-accepted test, was
369 employed to measure the distance between two independent distributions.

370 We compared the results of the chi-squared test for the turbulent heat fluxes computed using the ECMWF and ERA5
371 datasets. The decision rule for the χ^2 test was determined based on the level of significance, set at 0.05, and the
372 degrees of freedom, defined as $DF = N - np$, where N represents the number of bins and np is the number of
373 distribution parameters (i.e., 3 for both the ALD and skew-normal distribution). In the supplementary material we
374 show the maps of Chi-square test statistics (Fig. S5). The chi-squared results for the SH and LH fluxes computed
375 using the ECMWF dataset indicate that almost all surface grid points are well-fitted with the applied theoretical
376 PDFs, the ALD and skew-normal PDF. With the critical threshold of 33.92 (Elderton, 1902) for P values, we
377 observed a very few mismatches location near the coasts.

378

379 5. How do heat loss extremes contribute to the heat budget closure?

380 The heat budget closure problem is associated with achieving a net negative heat flux, as discussed before. We test
381 here the hypothesis that the negative long term mean negative heat budget of Table 1 for ECMWF data is correlated
382 to the extremes in heat losses during autumn-winter.

383 Figure 6 illustrates the Q_{net} basin average daily time series, revealing a value range varying between 200 and -500
384 $W m^{-2}$. Notably, the most pronounced extreme negative heat loss peaks, reaching up to 500 $W m^{-2}$ occur in the
385 winters of 2011, 2015 and 2017. They approximately coincide with western Mediterranean Deep Water formation
386 events, as documented in Escoudier et al. (2021). To identify and remove the potential extremes in our computed
387 Q_{net} time series, we apply the Interquartile Range (IQR) method which measures the spread of a dataset and
388 calculate the difference between the third quartile(Q3) and the first quartile (Q1). The IQR threshold is computed
389 by the difference between the 1st quartile (Q1) and 3rd Quartile (Q3) of the observed dataset:

390

$$391 \quad IQR = Q3 - Q1 \quad (17)$$

$$392 \quad \text{Threshold} = Q1 - k * IQR \quad (18)$$

393

394 We used different values for k to exclude the negative extremes, which correspond to the maximum heat losses.
395 These extremes values are replaced with long term yearly climatology values for the extreme heat losses days and
396 the long term mean neat heat budget Q_{net} is recomputed.

397 The resulting Q_{net} for different thresholds is displayed in Table 2 and the thresholds are shown in Fig. 7 together
398 with the daily seasonal climatology. If compared with the long term mean heat budget in Table 1 ($-3.6 W m^{-2}$) we
399 see that eliminating the winter extremes produces a smaller long term mean heat loss up to changing the sign to



positive values. We argue that this is reason why ECMWF and ERA5 have so different Q_{net} long term mean values, the low resolution of ERA5 does not allow for extreme heat losses in the winter. Furthermore, if we calculate the yearly mean value of the seasonal climatology, we obtain the value of $+4 \text{ W m}^{-2}$, which confirms again the importance of extremes in the heat budget closure of the Mediterranean Sea.

The Q_{net} could become an impact indicator of the Mediterranean steady state balance and be used to see if trends are working on the overall basin.

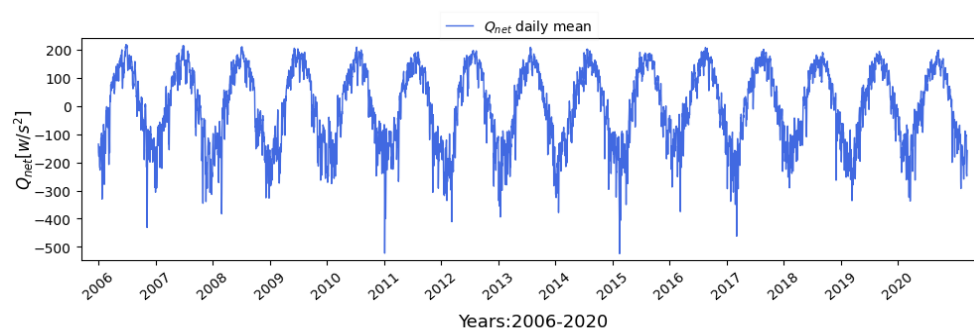


Figure 6: Basin averaged time series of the computed daily Q_{net} (units W m^{-2}) from the ECMWF computed heat fluxes, for the period 2006-2020.

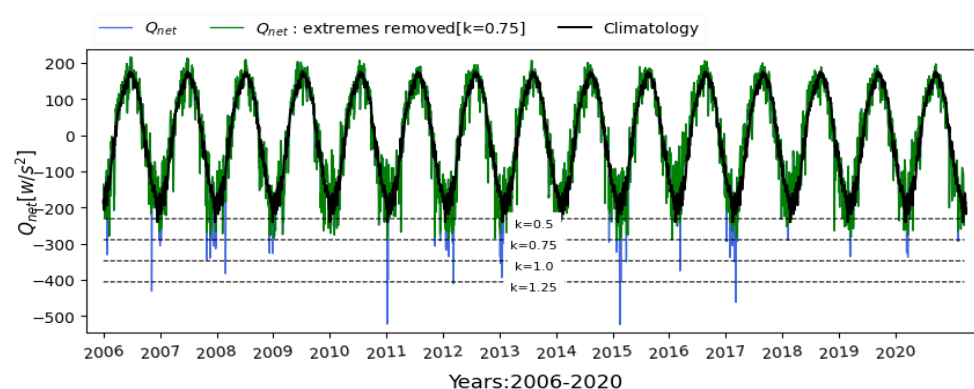


Figure 7: Time series of the basin averaged Q_{net} means, Q_{net} extremes removed, and long-term yearly climatology and four lower quantile boundary line marked with dashed lines using different k values [$k=1.25, 1, 0.75, 0.5$].



419

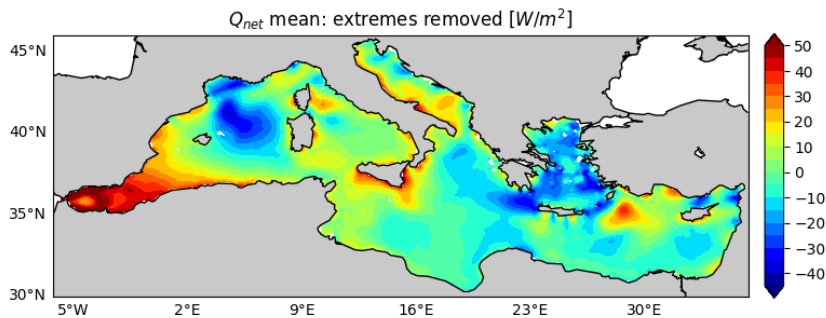
420 **Table 2: Different lower quantile boundary limits used to replace potential extremes and the resulting long-**
421 **term mean basin averaged Q_{net} values**

IQR lower boundary limit	Threshold value (W m^{-2})	$Q_{net}(\text{Wm}^{-2})$
K=1.25	405	-3.2
K=1.0	347	-2.5
K=0.75	289	-1
K= 0.5	231	2

422

423 The new spatial long-term means heat budget structure with the extremes removed choosing a threshold
424 of 289 (for $k=0.75$) is presented in the figure 8, which indicates extremes influence most the net heat
425 budget structures in the Mediterranean Sea (in comparison with Fig. 3a). Furthermore, the elimination
426 of extremes indicates that the net multi-year average of the heat flux in the Mediterranean Sea is connected
427 to extreme events occurring in the Gulf of Lion, the eastern Adriatic Sea and the southern Turkish shelves.

428



429

430 **Figure 8: The annual mean after the removal of extremes with significant reduction of negative heat fluxes**
431 **in the Gulf of Lion, Adriatic Sea and Aegean Sea regions.**

432

433

434

435

436

437

438

439



440 6. Discussion and conclusions

441

442 The primary motivation behind this investigation is to revisit the heat budget closure hypothesis from atmospheric
443 consolidated data sets that are nowadays used frequently to drive ocean models. For this analysis, we covered a 15-
444 year period from 2006 to 2020 with a daily time series frequency. The reason for the choice of this time range is
445 that ECMWF analyses became quite stable starting from 2006 while before the model was at coarse resolution, like
446 ERA5's model. Our strategy is to use the same bulk formula for the ERA5 and ECMWF data sets and compute the
447 long term mean heat budget. Our strategy is to use the same SST and the same bulk formula but different atmospheric
448 reanalysis and analysis surface variable data sets and compare the value of the long term mean heat budget in the
449 Mediterranean Sea.

450 Firstly, the heat budget of the Mediterranean Sea was analysed to examine average annual mean and seasonal
451 variations. The largest component of the heat budget is the net solar radiation (SW), followed by the latent heat
452 (LH), longwave radiation (LW), and then sensible heat (SH), as shown in the literature. All heat flux components
453 exhibit significant seasonality, as illustrated in Figure 3. Differences appear in the structure of the fluxes when
454 different atmospheric data sets are used, a conclusion aligning with a suggestion from Marullo et al. (2021) on the
455 sensitivity of LW estimates from the atmospheric dataset used to calculate fluxes.

456 The basin-average net heat flux, Q_{net} , was calculated to be $-3.6 \pm 1.3 \text{ W m}^{-2}$ for ECMWF analysis data while it is
457 $5 \pm 1.2 \text{ W m}^{-2}$ for ERA5 (Table 1). This finding supports the conclusion that heat budget closure hypothesis cannot
458 be satisfied with a relatively coarse reanalysis atmospheric data set. Our initial question was: is the Mediterranean
459 Sea in the past 15 years still losing heat at the surface? The answer is yes if we use a high-resolution ECMWF
460 atmospheric analysis.

461 Furthermore, we have demonstrated that the probability density of surface heat fluxes can be modelled and fitted
462 with a three-parameter PDF composed of a shape, a location, and a scale parameter. All the turbulent heat flux
463 components show asymmetric behaviour. There is encouraging agreement between the first two statistical moments
464 of the fitted PDF and the observed values. Kurtosis does not seem to be properly captured by the PDF used but our
465 time series is too short to arrive at a definitive conclusion. For the SH we demonstrate that the ALD PDF is generated
466 by the contributing distributions of wind speed (Weibull) and temperature difference, combined to form the heat
467 flux. We believe this is the first time that such kind of transformation is demonstrated.

468 Gulev and Belyaev (2012) applied the two-parameter Fisher–Tippett distribution (also known as the Gumbel
469 distribution) to monthly sensible and latent heat fluxes derived from NCEP–NCAR reanalysis fields. Their
470 approach focused on using the mean and standard deviation to estimate the distribution's location and scale
471 parameters relevant to extreme events. However, the Gumbel distribution has a fixed skewness, limiting its ability
472 to capture the contribution of rare, asymmetric extremes. In contrast, our study analyses anomalies from the
473 seasonal cycle using full probability distributions that allow for variable skewness. This better reflects the nature
474 of atmospheric and oceanic variables, which are often inherently skewed (Sardeshmukh and Penland, 2015), and is
475 essential for understanding the influence of extremes on the surface heat budget. Our findings show that
476 incorporating a shape parameter is key to accurately capturing distribution structure and preserving asymmetric



477 tails. This analysis provides a useful framework for validating surface flux products and assessing their variability,
478 particularly important given that surface fluxes are the dominant source of uncertainty in the Mediterranean net heat
479 balance (Jordà et al., 2017). Correctly estimating skewness is crucial, as a small number of extreme outliers,
480 especially during intense winter events, can disproportionately affect the basin-wide mean and determine whether
481 heat budget closure is achieved.

482 For the first time, we have investigated the effects of extreme heat losses in the Mediterranean Sea in the long term
483 mean basin averaged heat budget. The northern basin areas are the site of the largest heat losses (Gulf of Lion and
484 the Aegean Sea, Adriatic Sea and the Turkish southern coasts). Exclusion of the negative extremes in these areas
485 resulted in a change in the sign of long term mean heat loss. The threshold value that produces a positive basin
486 mean heat loss is 231 W m^{-2} . Thus, if the basin mean heat loss does not exceed this value, the basin is not in steady
487 state. This might be a good indicator of Mediterranean Sea heat content trends to be exploited in the future. Our
488 second initial question was: what is the cause of the Mediterranean Sea negative long-term mean heat budget? The
489 answer is that the long-term mean, basin averaged heat loss is due to winter extremes in the Northern regions of the
490 Mediterranean Sea.

491 In conclusion, understanding the characteristics and distributions of air-sea heat fluxes are crucial for gaining
492 insights into variations in the heat budget. Moreover, PDFs of heat fluxes that have been estimated in this study
493 will allow in the future to understand the importance of extreme events to compose the net negative heat budget.
494 The next steps could involve a machine learning study of air-sea flux bulk parametrizations for different atmospheric
495 data sets and coupled models, using as target the data set from this study.

496

497

498

499

500

501

502

503

504

505

506

507

508

509



510 **Author contributions**

511

512 MHG: development of the concept, literature review, writing, methodology, coding, formal analysis, wiring,
513 visualization. NP: conceptualization, review, writing, methodology. AN: conceptualization, writing, review. LM:
514 review, writing. SB: methodology, review. FM: methodology, review. FT: methodology, coding.

515

516 **Acknowledgments.**

517 This research has been funded from the University of Bologna under the Future Earth, Climate Change and Societal
518 Challenges PhD Program for MHG. Additionally, there was a partial support from the Edito-Lab HEU project for
519 MHG and NP.

520

521 **Conflict of interest Statement**

522 The authors declare no conflicting interests.



APPENDIX A

Here, we show that the characteristics of the SH flux distribution are due to the specific form of the heat flux as given by (10), i.e. a multiplication of two distributions, wind speed and temperature differences, that are described by a different distribution.

Let's indicate with $P(v*DT)$ the combined SH distribution of $Q(v)$ for wind speed and $R(DT)$ the temperature difference as in equation (09). Assuming that the two distributions are independent, the combined distribution is the product of Q and R . If we now define the variable $z=v*DT$, the new combined distribution on the heat flux variable z is given by the Mellin transform and convolution, described in Papoulis, A., & Pillai, S. U. (2002).

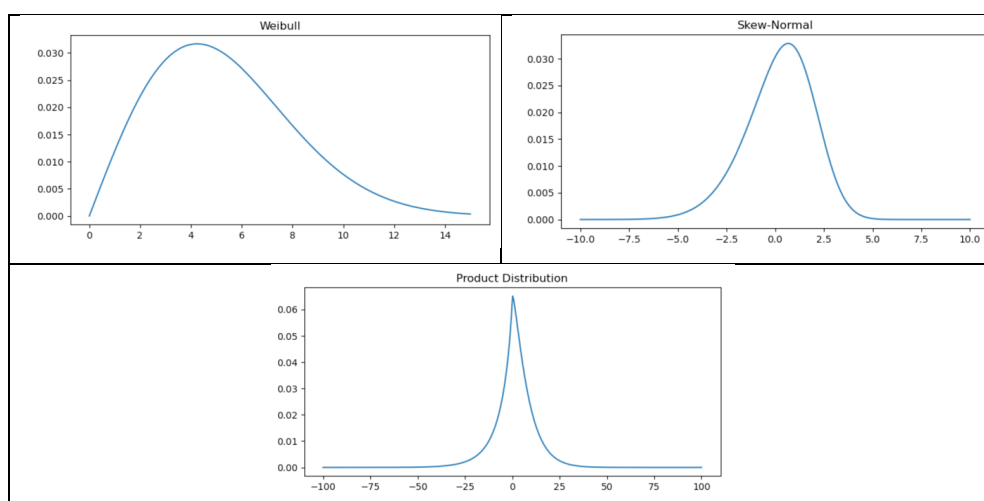


Figure A1: Histograms presenting the two original distributions, $Q(v)$ (upper left quadrant, units wind speed) and $R(DT)$ (upper right quadrant, units degrees C) and the combined distribution for SH flux in units of $W m^{-2}$. The parameters used for the two original distributions are: $k = 2.0$ for the Weibull shape, $\lambda = 6.0$ for the Weibull scale; $\alpha = -2.0$ for the Skew Normal shape, $\mu = 2.0$ for the Skew Normal location and $\omega = 2.5$ for the Skew Normal scale



APPENDIX B

The statistical moments for the skew-normal PDF are given by:

$$E(x) = \mu + \lambda \delta \sqrt{\frac{2}{\pi}} \quad (\text{B1})$$

$$\sigma^2 = \lambda^2 \left(1 - \frac{2\delta^2}{\pi}\right) \quad (\text{B2})$$

$$\mu_3 = (4 - \pi) \frac{(\delta \sqrt{2/\pi})^3}{2(1 - 2\delta^2/\pi)^{3/2}} \quad (\text{B3})$$

$$\mu_4 = 2(\pi - 3) \frac{\left(\delta \sqrt{\frac{2}{\pi}}\right)^4}{\left(1 - \frac{2\delta^2}{\pi}\right)^2} \quad (\text{B4})$$

where $\delta = \frac{\alpha}{\sqrt{1 + \alpha^2}}$. Since the expected value of the time series is zero, we deduce that:

$$\mu = -\lambda \delta \sqrt{\frac{2}{\pi}} \quad (\text{B5})$$

In other words, location and shape parameters have opposite signs since the scale parameter, λ , is always positive.

SH flux anomaly distribution was analysed with ALD PDF and its' statistical moments are given by:

$$\text{mean} = \mu + \frac{1 - \alpha^2}{\lambda \alpha} \quad (\text{B6})$$

$$\text{variance} = \frac{1 + \alpha^2}{\lambda^2 \alpha^2} \quad (\text{B7})$$

$$\text{Skewness} = \frac{2(1 - \alpha^6)}{(\alpha^4 + 1)^{3/2}} \quad (\text{B8})$$

$$\text{Kurtosis} = \frac{6(1 + \alpha^3)}{(1 + \alpha^4)^2} \quad (\text{B9})$$



565 **References**

566

567 Azzalini, A. (1985). A class of distributions which includes the normal ones. *Scandinavian journal of statistics*, 171-
568 178, <https://www.jstor.org/stable/4615982>

569

570 Bignami, F., S. Marullo, R. Santoleri, and M. E. Schiano (1995), Long wave radiation budget on the Mediterranean
571 Sea, *J. Geophys. Res.*, 100, 2501–2514, <https://doi.org/10.1029/94JC02496>
572

573 Bunker, A. F., H. Charnock, and R. A. Goldsmith. 1982. "A note on the heat balance of the Mediterranean and Red
574 Seas." *Journal of Marine Research* 40, (S), https://elischolar.library.yale.edu/journal_of_marine_research/1634

575

576 Béthoux, J. P. (1979). Budgets of the Mediterranean Sea-Their dependance on the local climate and on the
577 characteristics of the Atlantic waters. *Oceanologica acta*, 2(2), 157-163.

578

579 Béthoux, J. P., Gentili, B., & Tailliez, D. (1998). Warming and freshwater budget change in the Mediterranean since
580 the 1940s, their possible relation to the greenhouse effect. *Geophysical Research Letters*, 25(7), 1023-1026,
581 <https://doi.org/10.1029/98GL00724>

582

583 Criado-Aldeanueva, F., Soto-Navarro, F. J., & García-Lafuente, J. (2012). Seasonal and interannual variability of
584 surface heat and freshwater fluxes in the Mediterranean Sea: Budgets and exchange through the Strait of Gibraltar,
585 <https://dx.doi.org/https://doi.org/10.1002/joc.2268>

586

587 Castellari, S., Pinardi, N., & Leaman, K. (1998). A model study of air-sea interactions in the Mediterranean
588 Sea. *Journal of Marine Systems*, 18(1-3), 89-114, [https://doi.org/10.1016/S0924-7963\(98\)90007-0](https://doi.org/10.1016/S0924-7963(98)90007-0)

589

590 Cessi, P., Pinardi, N. and Lyubartsev, V., 2014. Energetics of semi enclosed basins with two-layer flows at the
591 strait. *Journal of physical oceanography*, 44(3), pp.967-979, <https://doi.org/10.1175/JPO-D-13-0129.1>

592

593 Cronin, M. F., Gentemann, C. L., Edson, J., Ueki, I., Bourassa, M., Brown, S., ... & Zhang, D. (2019). Air-sea fluxes
594 with a focus on heat and momentum. *Frontiers in Marine Science*, 6, 430, <https://doi.org/10.3389/fmars.2019.00430>

595

596 De Dominicis, M., Pinardi, N., Zodiatis, G., & Lardner, R. J. G. M. D. (2013). MEDSLIK-II, a Lagrangian marine
597 surface oil spill model for short-term forecasting—Part 1: Theory. *Geoscientific Model Development*, 6(6), 1851-
598 1869, <https://doi.org/10.5194/gmd-6-1851-2013>, 2013

599

600 Elderton, William Palin. (1902). "Tables for Testing the Goodness of Fit of Theory to Observation". *Biometrika*. 1
601 (2): 155–163, <https://www.jstor.org/stable/2331485>

602



- 603 Escudier, R., Clementi, E., Cipollone, A., Pistoia, J., Drudi, M., Grandi, A., Lyubartsev, V., Lecci, R., Aydogdu, A.,
604 Delrosso, D., Omar, M., Masina, S., Coppini, G., Pinardi, N., 2021. A high-resolution reanalysis for the
605 Mediterranean Sea. *Front. Earth Sci.* 9, 702285, <https://doi.org/10.3389/feart.2021.702285>
- 606
- 607 Fairall, C. W., Bradley, E. F., Hare, J. E., Grachev, A. A., & Edson, J. B. (2003). Bulk parameterization of air–sea
608 fluxes: Updates and verification for the COARE algorithm. *Journal of climate*, 16(4), 571-591,
609 [https://doi.org/10.1175/1520-0442\(2003\)016<0571:BPOASF>2.0.CO;2](https://doi.org/10.1175/1520-0442(2003)016<0571:BPOASF>2.0.CO;2)
- 610
- 611 Flecher, C., Naveau, P., Allard, D., & Brisson, N. (2010). A stochastic daily weather generator for skewed
612 data. *Water Resources Research*, 46(7), <https://doi.org/10.1029/2009WR008098>
- 613
- 614 Garrett, C., Outerbridge, R., & Thompson, K. (1993). Interannual variability in Mediterranean heat and buoyancy
615 fluxes. *Journal of Climate*, 900-910, <https://www.jstor.org/stable/26197277>
- 616
- 617 Gulev, S. K., & Belyaev, K. (2012). Probability distribution characteristics for surface air–sea turbulent heat fluxes
618 over the global ocean. *Journal of Climate*, 25(1), 184-206, <https://doi.org/10.1175/2011JCLI4211.1>
- 619
- 620 Hersbach, H., Bell, B., Berrisford, P., Hirahara, S., Horányi, A., Muñoz-Sabater, J., ... & Thépaut, J. N. (2020). The
621 ERA5 global reanalysis. *Quarterly Journal of the Royal Meteorological Society*, 146(730), 1999-2049.
- 622
- 623 Jordá, G., Von Schuckmann, K., Josey, S. A., Caniaux, G., García-Lafuente, J., Sammartino, S., ... & Macías, D.
624 (2017). The Mediterranean Sea heat and mass budgets: Estimates, uncertainties and perspectives. *Progress in*
625 *Oceanography*, 156, 174-208, <https://doi.org/10.1016/j.pocean.2017.07.001>
- 626
- 627 Korolev, V., Gorshenin, A., Gulev, S., & Belyaev, K. (2015). Statistical modeling of air-sea turbulent heat fluxes by
628 finite mixtures of Gaussian distributions. In *International Conference on Information Technologies and*
629 *Mathematical Modelling* (pp. 152-162). Springer, Cham, https://doi.org/10.1007/978-3-319-25861-4_13
- 630
- 631 Kara, A. B., Rochford, P. A., & Hurlburt, H. E. (2000). Efficient and accurate bulk parameterizations of air–sea
632 fluxes for use in general circulation models. *Journal of Atmospheric and Oceanic Technology*, 17(10), 1421-1438,
633 [https://doi.org/10.1175/1520-0426\(2000\)017<1421:EAABPO>2.0.CO;2](https://doi.org/10.1175/1520-0426(2000)017<1421:EAABPO>2.0.CO;2)
- 634
- 635 Large, W., & Yeager, S. G. (2009). The global climatology of an interannually varying air–sea flux data set. *Climate*
636 *dynamics*, 33(2), 341-364, <https://doi.org/10.1007/s00382-008-0441-3>
- 637
- 638 May, P. W. (1986). A brief explanation of Mediterranean heat and momentum flux calculations, NORDA Code
639 322. Nav Oceanogr Atmos Res Lab, 5.
- 640



- 641 Marullo, S., Pitarch, J., Bellacicco, M., Sarra, A. G. D., Meloni, D., Monteleone, F., ... & Santoleri, R. (2021). Air–
642 sea interaction in the central Mediterranean Sea: assessment of reanalysis and satellite observations. *Remote*
643 *Sensing*, 13(11), 2188.d; <https://doi.org/10.3390/rs13112188>
- 644
- 645 Matsoukas, C., Banks, A. C., Hatzianastassiou, N., Pavlakis, K. G., Hatzidimitriou, D., Drakakis, E., ... & Vardavas,
646 I. (2005). Seasonal heat budget of the Mediterranean Sea. *Journal of Geophysical Research: Oceans*, 110(C12),
647 <https://doi.org/10.1029/2004JC002566>
- 648
- 649 Papoulis, A., & Pillai, S. U. (2002). *Probability, Random Variables, and Stochastic Processes*, 4th Edition.
- 650
- 651 Payne, R. E. (1972). Albedo of the sea surface. *Journal of Atmospheric Sciences*, 29(5), 959-970,
652 [https://doi.org/10.1175/1520-0469\(1972\)029<0959:AOTSS>2.0.CO;2](https://doi.org/10.1175/1520-0469(1972)029<0959:AOTSS>2.0.CO;2)
- 653
- 654 Pettenuzzo, D., Large, W. G., & Pinardi, N. (2010). On the corrections of ERA-40 surface flux products consistent
655 with the Mediterranean heat and water budgets and the connection between basin surface total heat flux and NAO.
656 *Journal of Geophysical Research: Oceans*, 115(C6), <https://doi.org/10.1029/2009JC005631>
- 657
- 658 Pinardi, N., P. Cessi, F. Borile, and C.L. Wolfe, 2019: The Mediterranean Sea Overturning Circulation. *J. Phys.*
659 *Oceanogr.*, 49, 1699–1721, <https://doi.org/10.1175/JPO-D-18-0254.1>
- 660
- 661 Rabier, F., Järvinen, H., Klinker, E., Mahfouf, J. F., & Simmons, A. (2000). The ECMWF operational
662 implementation of four-dimensional variational assimilation. I: Experimental results with simplified physics.
663 *Quarterly Journal of the Royal Meteorological Society*, 126(564), 1143-1170,
664 <https://doi.org/10.1002/qj.49712656415>
- 665
- 666 Rosati, A., and K. Miyakoda (1988), A general circulation model for upper ocean simulation, *J. Phys. Oceanogr.*,
667 18, 1601–1626, [https://doi.org/10.1175/1520-0485\(1988\)018<1601:AGCMFU>2.0.CO;2](https://doi.org/10.1175/1520-0485(1988)018<1601:AGCMFU>2.0.CO;2)
- 668
- 669 Ruiz, S., Gomis, D., Sotillo, M. G., & Josey, S. A. (2008). Characterization of surface heat fluxes in the
670 Mediterranean Sea from a 44-year high-resolution atmospheric data set. *Global and Planetary Change*, 63(2-3), 258-
671 274, <https://doi.org/10.1016/j.gloplacha.2007.12.002>
- 672
- 673 Small, R. J., Bryan, F. O., Bishop, S. P., & Tomas, R. A. (2019). Air–sea turbulent heat fluxes in climate models
674 and observational analyses: What drives their variability? *Journal of Climate*, 32(8), 2397-2421,
675 <https://doi.org/10.1175/JCLI-D-18-0576.1>
- 676
- 677 Sverdrup, H. U., Johnson, M. W., and Fleming, R. H. (1942). *The Oceans, Their Physics, Chemistry, and General*
678 *Biology*, Prentice-Hall, New York, <http://ark.cdlib.org/ark:/13030/kt167nb66r/>
- 679



- 680 Sanchez-Gomez, E., Somot, S., Josey, S. A., Dubois, C., Elguindi, N., & Déqué, M. (2011). Evaluation of
681 Mediterranean Sea water and heat budgets simulated by an ensemble of high-resolution regional climate
682 models. *Climate dynamics*, 37(9), 2067-2086, <https://doi.org/10.1007/s00382-011-1012-6>
683
- 684 Song, X., & Yu, L. (2017). Air-sea heat flux climatologies in the Mediterranean Sea: Surface energy balance and its
685 consistency with ocean heat storage. *Journal of Geophysical Research: Oceans*, 122(5), 4068-4087,
686 <https://doi.org/10.1002/2016JC012254>
- 687
- 688 Sardeshmukh, P. D., & Penland, C. (2015). Understanding the distinctively skewed and heavy-tailed character of
689 atmospheric and oceanic probability distributions. *Chaos: An Interdisciplinary Journal of Nonlinear Science*, 25(3),
690 <https://doi.org/10.1063/1.4914169>
691
- 692 Tian, F., von Storch, J. S., & Hertwig, E. (2017). Air-sea fluxes in a climate model using hourly coupling between
693 the atmospheric and the oceanic components. *Climate Dynamics*, 48(9), 2819-2836, [https://doi.org/10.1007/s00382-](https://doi.org/10.1007/s00382-016-3228-y)
694 [016-3228-y](https://doi.org/10.1007/s00382-016-3228-y)
- 695
- 696 Tibshirani, R. J., & Efron, B. (1993). An introduction to the bootstrap. *Monographs on statistics and applied*
697 *probability*, 57(1), 1-436,
698
- 699 Wallace, J. M., & Hobbs, P. V. (2006). *Atmospheric science: an introductory survey* (Vol. 92), Elsevier.
- 700
- 701 Yu, K., & Zhang, J. (2005). A three-parameter asymmetric Laplace distribution and its extension. *Communications*
702 *in Statistics—Theory and Methods*, 34(9-10), 1867-1879, <https://doi.org/10.1080/03610920500199018>